Measurement and modeling of $Ar/H_2/CH_4$ arc jet discharge chemical vapor deposition reactors II: Modeling of the spatial dependence of expanded plasma parameters and species number densities

Yu. A. Mankelevich[a)]
Nuclear Physics Institute, Moscow State University, 119992 Moscow, Russia

M. N. R. Ashfold and A. J. Orr-Ewing
School of Chemistry, University of Bristol, Cantock's Close, Bristol BS8 1TS, United Kingdom

(Received 26 March 2007; accepted 31 July 2007; published online 28 September 2007)

Detailed methodology and results are presented for a two-dimensional (r,z) computer model applicable to dc arc jet reactors operating on argon/hydrogen/hydrocarbon gas mixtures and used for chemical vapor deposition of micro- and nanocrystalline diamond and diamondlike carbon films. The model incorporates gas activation, expansion into the low pressure reactor chamber, and the chemistry of the neutral and charged species. It predicts the spatial variation of temperature, flow velocities and number densities of 25 neutral and 14 charged species, and the dependence of these parameters on the operating conditions of the reactor such as flows of H_2 and CH_4 and input power. Selected outcomes of the model are compared with experimental data in the accompanying paper [C. J. Rennick *et al.*, J. Appl. Phys. **102**, 063309 (2007)]. Two-dimensional spatial maps of the number densities of key radical and molecular species in the reactor, derived from the model, provide a summary of the complicated chemical processing that occurs. In the vortex region beyond the plume, the key transformations are $CH_4 \rightarrow CH_3 \leftrightarrow C_2H_2 \leftrightarrow$ large hydrocarbons; in the plume or the transition zone to the cooler regions, the chemical processing involves $C_2H_x \leftrightarrow (CH_y$ and $CH_z)$, $C_3H_x \leftrightarrow (CH_y$ and $C_2H_z)$, $(C_2H_y$ and $C_2H_z) \leftrightarrow C_4H_x \leftrightarrow (CH_y$ and $C_3H_z)$. Depending on the local gas temperature T_g and the H/H_2 ratio, the equilibria of H-shifting reactions favor C, CH, and C_2 species (in the hot, H-rich axial region of the plume) or CH_2, C_2H, and C_2H_2 species (at the outer boundary of the transition zone). Deductions are drawn about the most abundant C-containing radical species incident on the growing diamond surface (C atoms and CH radicals) within this reactor, and the importance of chemistry involving charged species is discussed. Modifications to the boundary conditions and model reactor geometry allow its application to a lower power arc jet reactor operated and extensively studied by Jeffries and co-workers at SRI International, and comparisons are drawn with the reported laser induced fluorescence data from these studies. © *2007 American Institute of Physics*. [DOI: 10.1063/1.2783891]

I. INTRODUCTION

The accompanying paper[1] described the latest results and analysis of our extensive experimental studies of the properties of a 6.4 kW dc arc jet reactor operating on an $Ar/H_2/CH_4$ gas mixture and used to deposit thin films of polycrystalline diamond. This reactor has been the subject of many prior experimental and computational studies,[2–8] and comparisons of spectroscopic data with the outputs of a computer model have enabled the model to develop in sophistication and accuracy. In turn, the insights provided by analysis of the model results inform our understanding of the physical and chemical processes that occur in the nozzle, gas expansion, and free-plume region of this and, by extension, other arc jet reactors. Here, we describe in detail the various components of the model, which builds upon prior computational studies of diamond deposition arc jet reactors[3,4,6,9,10] and our previous work on Ar/H_2 expansions.[7,8] The latter improvements come through the incorporation of the H/C chemistry ensuing from CH_4 addition to the plume, an improved treatment of the role of charged species, and several other important refinements. The model was tested by comparison with experimental data, and the preceding paper presents selected outcomes of this intercomparison. Although some discrepancies remain between absolute values and spatial profiles of calculated and measured number and column densities of $H(n=2)$, C_2, and CH, the level of agreement serves to justify the key features of the model. In this paper, further details are provided of the calculated number densities of numerous species (for example, H atoms, C atoms, C_2, C_2H, CH, C_3, CH_x, C_2H_2, CH_4, and electrons) and their dependence on spatial location in the plume and the operating parameters of the reactor. From the radial variations of number densities of several radical species in proximity to the substrate, we can speculate about the relative importance of these compounds on the growth of polycrystalline diamond films. The versatility of the model is demonstrated by the calculations conducted for the conditions of operation of a lower power dc arc jet reactor operated and extensively studied by Jeffries and co-workers at SRI International.[11–16]

[a)]Author to whom correspondence should be addressed. Electronic mail: ymankelevich@mics.msu.edu

II. COMPUTER MODELING OF DC ARC JET CVD REACTORS

A. Overview of the model

The improved computer simulation of the arc jet discharge chemical vapor deposition (CVD) reactor consists of three main phases: (I) determination of plasma parameters in the region of the dc arc discharge, the intermediate torch head chamber, and at the nozzle into the reaction chamber (we focus on the primary N-torch nozzle); (II) a two-dimensional model of the expansion of the plasma into the reaction chamber; and (III) incorporation of C/H/Ar plasma chemistry and gas-surface deposition processes at the substrate. The gas temperature, gas pressure, flow velocity, and degree of ionization of an activated Ar/H_2 feedstock gas are calculated in phase (I) from power and mass balances and experimental measurements of the difference between the supplied power and the power coupled into the plasma. The corresponding plasma and flow parameters at the primary nozzle are used as boundary conditions for the two-dimensional model of the expanding plasma.

Phases (I) and (II) for an argon-hydrogen plasma have been fully described in our preceding paper[7] and are only briefly summarized here. The first two phases of the model address the activation within the primary nozzle of an Ar/H_2 feedstock gas flow and the expansion of the resultant, partially ionized mixture into the reaction chamber. The model incorporates analytical procedures for the argon excitation in the region of the dc arc discharge, based on the energy deposited and use of the Saha equation to compute the degree of ionization, and the results of mixing with further Ar and H_2 flow in the intermediate nozzle chamber (including complete thermal dissociation of H_2). The treatment includes the expansion of the Ar, H, Ar^+, H^+, and electrons through the primary nozzle into the reactor chamber, formation of a shock front at small z, ~6 mm, generation of the plasma plume, its interaction with nearby cold gas, and various plasma-chemical and radiative transfer processes.

This paper focuses on the incorporation of the consequences of downstream addition of CH_4 to the plume, which is described in greater detail here. The associated chemical kinetics model includes 25 neutral and 15 charged species, more than 170 neutral reactions (direct and reverse), and 110 reactions with charged species. The key atoms, radicals, and molecules are C, CH, $^3CH_2$, $^1CH_2$, CH_3, CH_4, $C_2(X)$, $C_2(a)$, C_2H, C_2H_2, C_2H_3, C_2H_4, C_2H_5, C_2H_6, C_3, C_3H, C_3H_2, C_4, C_4H, C_4H_2, H, H(n=2), H(n=3), H_2, and Ar (a limited number of calculations were carried out for an expanded set of neutral species also including the heavier hydrocarbons C_3H_3, C_5H, C_6H, and C_6H_2). The charged species that are included are electrons, ions Ar^+, ArH^+, H^+, the negative ion H^-, and 10 hydrocarbon ions CH_y^+ (y=0–3), $C_2H_y^+$ (y=0–3), and $C_3H_y^+$ (y=0,1). Thermochemical data and the reaction kinetics data are taken from the GRI-Mech mechanism[17] (for H, H_2, CH_y, and C_2H_y reactions), pyrolysis mechanisms of C_2H_2 and CH_4 (for reactions up to C_4H_y compounds; C_4H_y is treated as a sink representing all higher hydrocarbons which are not explicitly described), and additional electronic state specific rates for $C_2(a)$ and $C_2(X)$ reaction and interconversion. In addition, atomic hydrogen recombination at the reaction chamber walls, with a probability γ=0.15 that is typical for metal surfaces,[18] is incorporated along with the following gas-surface processes at the substrate: atomic hydrogen recombination and sinks of CH_x, x=0–3 and C_2H_x, x=0–2.[19] The complete plasma-chemical reaction mechanism is provided as electronic supplementary information.[25] The temperature dependence of chemical reaction rates and thermochemical data should capture not only the chemistry up to 5000–6000 K in high power plasma reactors (corresponding to the well-studied range of temperatures arising in combustion), but also the higher temperature range above 6000 K, for which data are more scarce. Several aspects of the coupled chemistry and flow are discussed in this section. Comparisons of the model outputs with experimental data for the Bristol arc jet are presented in the accompanying paper[1] and for the SRI reactor in Sec. III.

To simulate the plasma expansion and formation of a plasma plume, the conservation equations for mass, species, energy, and radial and axial momenta were numerically integrated, simultaneously, using thermal and caloric equations of state and initial and boundary conditions in two dimensions, i.e., the cylindrical (r,z) coordinate space. The calculations incorporate heat, mass and radiation transfer, formation of a shock wave and gas flow recirculation, plasma-chemical kinetics, gas viscosity, diffusion, thermodiffusion, and barodiffusion (species diffusion due to a pressure gradient[20]) processes. Power-law temperature dependences as approximations of tabular data are used for the viscosity and thermal conductivity of the Ar/H mixture.[7] Neutral species thermodiffusion and diffusion (D) coefficients are calculated for different Ar/H/C mixtures using species specific Lennard-Jones parameters,[21] and diffusion coefficients are approximated as $D_i=a_iT^{1.7}/P$,[20] where a_i is a constant for species i. Charged species diffusion is ambipolar for the arc jet conditions, and ion diffusion fluxes and coefficients in a multicomponent mixture are calculated taking into account the energy dependence of various ion-neutral and ion-charged species collisions.[22]

The outcomes of this phase of the calculations are gas temperature, gas pressure, flow velocities, mole fractions, and number densities of plasma species, with two-dimensional (r,z) resolution. A positive column plasma in a high (atmospheric) pressure arc discharge is a dense hot equilibrium system,[22] so the electron temperature in the expanded plasma is taken to be the same as that of the heavy particles at the same location. The explicit conservative numerical integration scheme employed time steps of 6–20 ns and a grid size of Δr=0.5 mm in r and Δz=2.1 mm in z and continued until steady state conditions were attained. A limited number of test calculations were carried out for Δz=1 mm to check that the numerical results were insensitive to the larger chosen Δz. The reactor chamber is approximated as two cylinders in series, with respective radii of 19 and 72.5 mm and lengths of 82 and 92 mm. The center of the substrate, a disc with radius of 13 mm, is located at $(r=0,z_s)$. In this study, the base value of z_s was 155 mm to

match the experimental configuration. In all the calculations, the (water-cooled) substrate temperature was constrained to be 1200 K.

B. Further details and refinements of the model

Several modifications and corrections have been made in the present version of the two-dimensional model. First, barodiffusion[20] has been taken into account as an additional term in species mass diffusional fluxes j_i. For a two-component mixture, diffusional, thermodiffusional, and barodiffusional terms in $j_{i=1}$ are expressed as follows:[20]

$$j_1 = \frac{m_1 m_2}{m_{12}} D_{12} N \left[\nabla X_1 + \frac{k_{T1}}{T} \nabla T + \frac{(m_2 - m_1) X_1 X_2}{m_{12} P} \nabla P \right]. \tag{1}$$

Here, T, N, and P are the gas temperature, the total number density, and pressure, respectively, m_i and $X_i = N_i/N$ are the ith species mass and mole fractions, $m_{12} = m_1 X_1 + m_2 X_2$, and D_{12} and k_{T1} are the diffusional and thermodiffusional coefficients. The most prominent effects of barodiffusion are observed for atomic hydrogen near the nozzle and in the region of the shock front. In particular, H-atom mole fractions X_H just after the shock front are increased by factors of 2–3 compared with the initial mole fraction X_H^0 at the primary nozzle ($X_H \sim 3X_H^0$ for $X_H^0 = 6\%$ and $X_H \sim 2X_H^0$ for $X_H^0 = 20\%$). Quantitatively, similar H-atom behavior was experimentally observed by Mazouffre *et al.*,[23] and we suggest that this anomalous behavior is more likely caused by barodiffusional processes rather than from any plasma-surface interactions as proposed in Ref. 23.

A second significant modification is that H^+ ions are assumed to be present in the expanded plasma. As was estimated in our earlier work,[7] the residence time of H atoms in the hottest core region of the plasma stream in the intermediate nozzle chamber is ~30% of the characteristic ionization time; we therefore assume that the H^+ mole fraction X_{H+} in the plasma at the primary nozzle is about 30% of the equilibrium Saha values, e.g., $X_{H+} \sim 0.67\%$ for a base H_2 flow rate of 1.8 SLM (SLM denotes liter per minute at STP) and a gas temperature of $T = 12\,100$ K. Hydrogen ions are long-lived species in the hot plume because of low recombination rates (requiring three-body mechanisms) and an absence of fast charge transfer processes with the main plume species (Ar and, downstream, H_2) because the H-atom ionization potential is less than those of H_2 and Ar. Thus, H^+ ions survive in the plume and affect $H(n=2)$ concentrations downstream where the Ar^+ ion concentrations have fallen to zero as a result of their charge transfer reactions with H_2 molecules,

$$Ar^+ + H_2 \rightarrow ArH^+ + H. \tag{2}$$

This fast reaction (its rate coefficient, $k = 1.4 \times 10^{-9}$ cm^3 s^{-1} is ~10^4 times bigger than the rate coefficient of H_2 thermal dissociation, $H_2 + Ar \rightarrow 2H + Ar$, at a gas temperature $T = 6000$ K) suppresses the H_2 concentrations in the plume. The ion kinetics in a H/Ar plasma and radiation transfer and reabsorption via the $H(n=2) \leftrightarrow H(n=1)$ resonance line have been analyzed in our previous papers.[7,8] Radiation transfer is an important mechanism for the loss of excited $H(n>2)$ atoms, with consequences for ion kinetics, including ArH^+ ion production, and it was simulated previously by incorporation of C_{ij} coefficients into the calculations (where C_{ij} is a probability of the radiation from grid cell i being absorbed in cell j).[8] In the present calculations, the appropriate C_{ij} coefficients were calculated using a high resolution division (into 400 frequency intervals) of the (Voigt profile) emission and absorption line shapes. In the presence of a hydrocarbon process gas, the suppressed H_2 concentration will affect the C_xH_y transformations. In addition, various $C_xH_y^+$ ions with low ionization potentials (~9–13 eV) will appear in the plume as a result of charge transfer reactions between primary ions, Ar^+ and H^+, and C_xH_y species, e.g.,

$$Ar^+ + C_xH_y \rightarrow C_xH_y^+ + Ar, \tag{3}$$

$$Ar^+ + C_xH_y \rightarrow C_xH_{y-1}^+ + H + Ar, \tag{4}$$

$$H^+ + C_xH_y \rightarrow C_xH_y^+ + H, \tag{5}$$

$$H^+ + C_xH_y \rightarrow C_xH_{y-1}^+ + H_2. \tag{6}$$

The resulting $C_xH_y^+$ ions can also participate in further charge transfer reactions with C_xH_y species and are destroyed in dissociative recombination reactions with electrons, such as

$$C_xH_y^+ + e \rightarrow C_xH_{y-1} + H(n). \tag{7}$$

Calculations show that the concentration of the most abundant carbon-containing ion, C^+ (present at high levels because of its low electron-ion recombination rate) reaches $\sim 2.9 \times 10^{12}$ cm^{-3}, whereas the maximum concentrations of other $C_xH_y^+$ ions (e.g., CH^+, CH_3^+, and $C_2H_3^+$) are lower than $\sim 2 \times 10^{12}$ cm^{-3}. All of these values are much lower than the concentrations of primary ions at the nozzle (Ar^+ $\sim 4 \times 10^{16}$ cm^{-3} and $H^+ \sim 3 \times 10^{15}$ cm^{-3}), and the most important effect of the hydrocarbon ion kinetics on the neutral C_xH_y species transformations is the loss of C_xH_y species in the charge transfer reactions (3)–(6). This loss becomes dominant for some species, e.g., C_2 molecules, in regions of the plume where the H_2 concentration is much lower than the Ar^+ concentration, and such conditions are realized over the whole plume length at low H_2 flow rates ($F_{H_2} \leqslant 0.5$ SLM) and in the conical part of the plume at small z for high H_2 flow rates ($F_{H_2} \geqslant 1$ SLM, see below). In addition, the $C_xH_y^+$ ions enhance the total rate of ion-electron recombination and loss of primary ions, compressing the radial profiles of electrons and ArH^+ ions and, as a consequence, affecting $H(n>1)$ number density distributions [because $ArH^+ + e \rightarrow Ar + H(n)$ reactions are an important source of excited $H(n=2,3)$ atoms]. There is some additional loss of primary ions by recombination with negative ions, as illustrated by the reduction of H^+ ion concentrations. We only considered the effects of H^- ions, as these are among the most abundant negative ions under standard operating conditions. For base reactor conditions, the maximum concentrations of H^- ($\sim 3 \times 10^{12}$–7×10^{12} cm^{-3}) occur in the conical part of the plume at $z < 100$ mm, where the number densities of other nonprimary ions are also the greatest. H^- ion concentrations are

controlled by a balance of production by dissociative electron attachment to H_2 molecules and loss by detachment in collisions with electrons, associative detachment in collisions with H atoms, and recombination with positive ions.

As a third modification, the numerical approximation of power balance was corrected. In the previous version of the numerical model, the finite difference approximation of the boundary conditions at the primary nozzle underestimated the power coupled into the plasma. The revised two-dimensional model incorporates a much-improved treatment of the power utilization within the plasma. In our previous paper,[7] we developed an analytical approach that allows determination (when provided with experimental measurements of power losses) or estimation of plasma parameters (temperature, pressure, ionization degree, and flow velocity) at the exit of the primary nozzle of the Bristol (or any other) arc jet reactor as a function of known experimental data of species flow rates and input power. For input flows of H_2 and Ar, ${F_{H_2}}^0$ and ${F_{Ar}}^0$ (specified in $cm^3\ s^{-1}$ at STP, denoted as SCCS), user-specified total input power P_{total}, and measured power losses P_{loss} (both in W), we determined the gas temperature T (K), the total number density N (cm^{-3}), the total flow rate F (cm^3/s), and the species mole fractions X_i at the primary nozzle to be related via[7]

$$N = \frac{N^0(m_{H_2}{F_{H_2}}^0 + m_{Ar}{F_{Ar}}^0)}{S'\sqrt{\gamma kT}\sqrt{m_H(X_H + X_{H^+}) + m_{Ar}(X_{Ar} + X_{Ar^+})}}, \tag{8}$$

$$F(\mathrm{cm^3\ s^{-1}}) = \frac{(2{F_{H_2}}^0 + {F_{Ar}}^0)}{(1 - X_e)}\frac{N^0}{N}, \tag{9}$$

$$X_H = \frac{2{F_{H_2}}^0 N^0}{FN} - X_{H^+}, \tag{10}$$

and

$$X_{Ar} = \frac{{F_{Ar}}^0 N^0}{FN} - X_{Ar^+}, \tag{11}$$

where N^0 (cm^{-3}) is the number density at STP, $\gamma = C_p/C_v$ is a ratio of heat capacities, and k is the Boltzmann constant. The effective area of the nozzle aperture, S', is smaller than the physically measured cross-sectional area of the orifice, S, because of edge effects on the gas flow, and $S'/S \sim 0.85$. Charged species mole fractions X_{Ar^+}, X_{H^+}, and $X_e = X_{Ar^+} + X_{H^+}$ can be estimated at any gas temperature using the Saha equation. The temperature T is determined from power balance arguments,

$$\frac{3}{2}kT = \frac{(P_{total} - P_{loss}) \times 10^7}{FN} - \left[\frac{1}{2}X_H D_0(H_2) + I_{Ar}X_{Ar+} + I_H X_{H+}\right] + T_0\left({C_V}^0 {X_{H_2}}^0 + \frac{3}{2}k{X_{Ar}}^0\right), \tag{12}$$

where $\frac{1}{2}D_0(H_2)$ gives the heat of formation of a H atom in terms of the bond dissociation energy of H_2 (complete dissociation of H_2 is implicit), and I_{Ar} and I_H are the ionization energies of argon and atomic hydrogen. The parameters of the feed gas mixture ${C_V}^0$, ${X_{H_2}}^0$, ${X_{Ar}}^0$, and T_0 are, respectively, the heat capacity $[{C_V}^0(\mathrm{erg/K}) \sim 2.47k]$ and mole fraction of molecular hydrogen, the argon mole fraction, and the initial gas temperature. Note that the last term of Eq. (12) was neglected in our prior analysis.[7]

The model does not explicitly simulate the behavior of the plume in the thin boundary layer above the substrate. For typical gas flow conditions above the boundary layer (flow velocity $v_r \sim 10^5$ cm/s, gas density $\sim 7 \times 10^{-6}$ g/cm^3, gas temperature $\sim$6000 K), the thermal boundary layer thickness is estimated to be $\delta\,(\mathrm{cm}) \leqslant 0.1{R_s}^{1/2}$.[20] $R_s = 1.3$ cm is the substrate radius, and δ is comparable to, or lower than, the chemical mean free path for hydrocarbon species. The number densities of radicals computed for the region just preceding the boundary layer are thus taken to be representative of the number densities at the surface of the substrate, allowing inferences to be drawn about the chemical identity of the principal contributors to growth of diamond films. The extreme temperature gradient across the narrow boundary layer, whose thickness is only $\sim$70 elastic collision mean free paths, and the high plume velocity, which is comparable to Ar atom thermal velocities, suggest that local thermal equilibrium will not be established, preventing integration of a chemical mechanism with temperature-dependent reaction rates. In their model of diamond CVD, Yu and Girshick[10] considered chemical transformations within a boundary layer, and the effect of the thickness of this layer on the dominant diamond growth precursor species; their model, however, treated an atmospheric pressure plasma for which collisions in the boundary layer will be much more frequent than for the low pressure arc jets considered here.

C. Outcomes of the model

Equations (8)–(12) provide a detailed specification of the conditions prevailing in the throat of the primary nozzle, a schematic diagram of which is provided in Fig. 1 of Ref. 7. For example, under the base operating conditions, such as are favored for CVD diamond growth conditions (i.e., parameters for the N torch of $P_{total} \sim 6250$ W, ${F_{Ar}}^0 = 190$ SCCS (11.4 SLM) and ${F_{H_2}}^0 = 30$ SCCS (1.8 SLM), and a power $P_{total} - P_{loss} = 4450$ W coupled into the N-torch plasma), we find $T = 12\,100$ K and gas pressure $P \sim 900$ Torr; the gas velocity at the throat of this nozzle (denoted by NZRC in Ref. 7), where the cross-sectional diameter is 2.5 mm, will be $\sim$2.5 km/s. The preceding analysis also gives insight into the utilization of the high input power (corresponding to $\sim$5 eV per particle): ionization is the dominant sink of this power (consuming $\sim$2100 W, and causing a degree of ionization, $X_e = 0.1$). H_2 dissociation accounts for $\sim$670 W, and the balance is partitioned into thermal energy of the constituent particles.

The fully developed two-dimensional model was used for systematic study of the Bristol (see accompanying paper[1]) and SRI (Sec. III) dc arc jet reactors under various operation conditions to reveal key plasma-chemical and transport processes, to compare with ours and others' published experimental data, and to resolve several surprising experimental observations and challenges. In the Bristol CVD reactor, for example, the model calculations clarify (i)

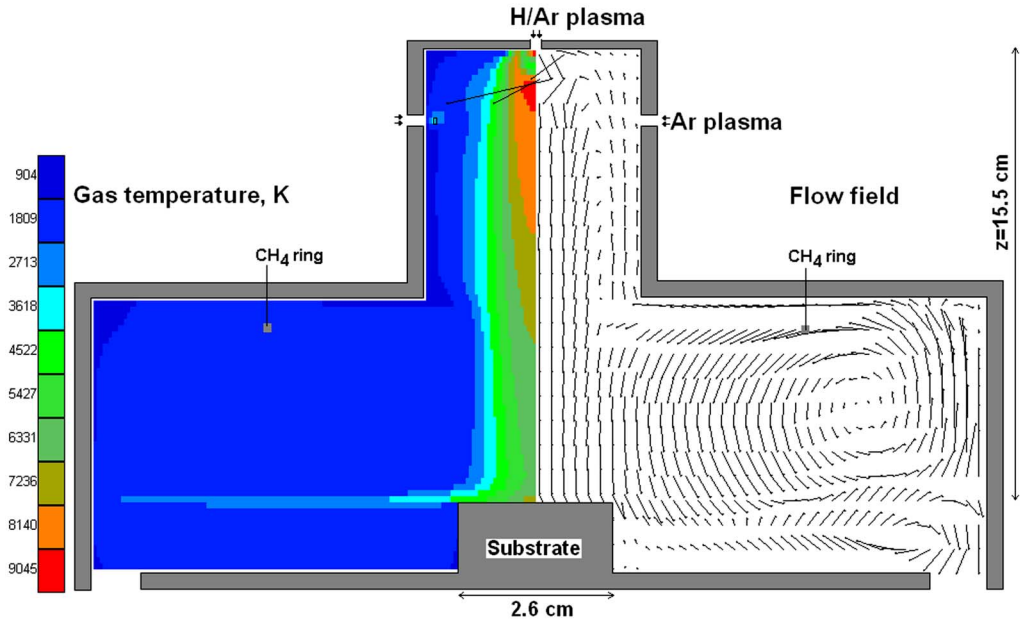

FIG. 1. Calculated temperature and gas flow profiles for the Bristol arc jet reactor operating under base conditions (see text for details). The primary nozzle is at the top center of the figure and the substrate at the bottom center. Left: two-dimensional temperature profiles, $T(r,z)$. Right: two-dimensional (r,z)-dependent gas velocities; the arrows show the directions of flow and are indicative of (but not directly proportional to) the flow velocities.

the observed thousandfold drop of detected H-α emission with increased H_2 flow rates (for 0.5 and 1.8 SLM), which was reported in Ref. 7; (ii) the question of how to treat measured column densities and rotational temperatures of CH and $C_2(a)$ in conditions of sharp gradients of temperature and species number densities, addressed in detail in the accompanying paper; (iii) which species are most likely to be responsible for the observed, extremely high ($\sim$100 μm/h) and nonuniform diamond film growth rates; and (iv) an apparent increase in electron number density with CH_4 flow rates, contrary to the decrease expected because of enhanced recombination rates of produced hydrocarbon ions, which will be discussed further below.

To illustrate the global heat and mass transfer processes occurring in the Bristol reactor, Fig. 1 shows two-dimensional (r,z) plots of the calculated T_{gas} and flow field for the base operating conditions (i.e., $F_{H_2}{}^0=1.8$ SLM and $F_{Ar}{}^0=11.4$ SLM flowing through the N torch, with a further $F_{CH_4}{}^0=80$ SCCM (SCCM denotes cubic centimeter per minute at STP) entering through the downstream injection ring, and a total power $W=4450$ W coupled into the N-torch plasma). The hot central core of the jet is strikingly evident in the former plot, as are a local minimum at small z and the rapid temperature rise within $\sim$1 cm of the substrate. The arrow lengths in the flow field plot are merely indicative of, and not directly proportional to, the absolute velocities. Nonetheless, this plot clearly illustrates the directed flow from the nozzle to the substrate and the importance of gas recirculation through the main body of the chamber and back into the narrower bore section. Such recirculation is crucial for efficient processing of hydrocarbon gases injected into the reactor when used for diamond CVD because the annulus, through which hydrocarbon process gas is injected, is located within the recirculation vortex.

The gas temperature distribution (consisting of a hot plume, a transition zone, and a cold surrounding gas) and interaction of the hot plasma with the cold gas generate extremely complicated and nonuniform distributions of all species concentrations. As an example, Fig. 2 shows the calculated two-dimensional mole fraction profiles of some important species C, CH, $C_2(a)$, C_2H_2, H, and H_2. Figures 1 and 2 clearly demonstrate that experimentally measured temperatures, obtained by line-of-sight spectroscopy, should be treated with special care (issue ii). Indeed, a measured $C_2(a)$ rotational temperature characterizes the plume boundary temperature rather than higher temperatures near the z axis ($r\sim0$). In contrast, CH rotational temperature measurements probe the hotter central regions and should be higher than $C_2(a)$ rotational temperatures, but still lower than the maximum axial temperatures. Experimental and calculated rotational temperatures, the latter averaged over the radial direction, at distances $z=145-120$ mm (i.e., $d=10-25$ mm from the substrate) confirm these observations: the temperature derived from rotational structure in the C_2 Swan-band experimental absorption spectrum is $T_{exp}[C_2(a)]\sim3300$ K, whereas the temperature derived from rotationally resolved CH spectra is $T_{exp}(CH)\sim4000$ K; from the two-dimensional model outputs, the corresponding values are $T_{calc}[C_2(a)]=3870$ K and $T_{calc}(CH)=4300-4670$ K.

Figures 1 and 2 also allow the main stages of the chemical processing, and the regions in which they occur, to be traced. CH_4 is released from the injection ring into the recirculation vortex region and is very rapidly decomposed by reaction with abundant H atoms (with local concentrations of $\sim5\times10^{14}$ cm^{-3}) under conditions of elevated Ar/H_2 gas temperatures ($\sim$1300–1800 K). The CH_3 radicals so produced undergo further chemical transformations into C_2H_2, which is more stable under these conditions, as well as other

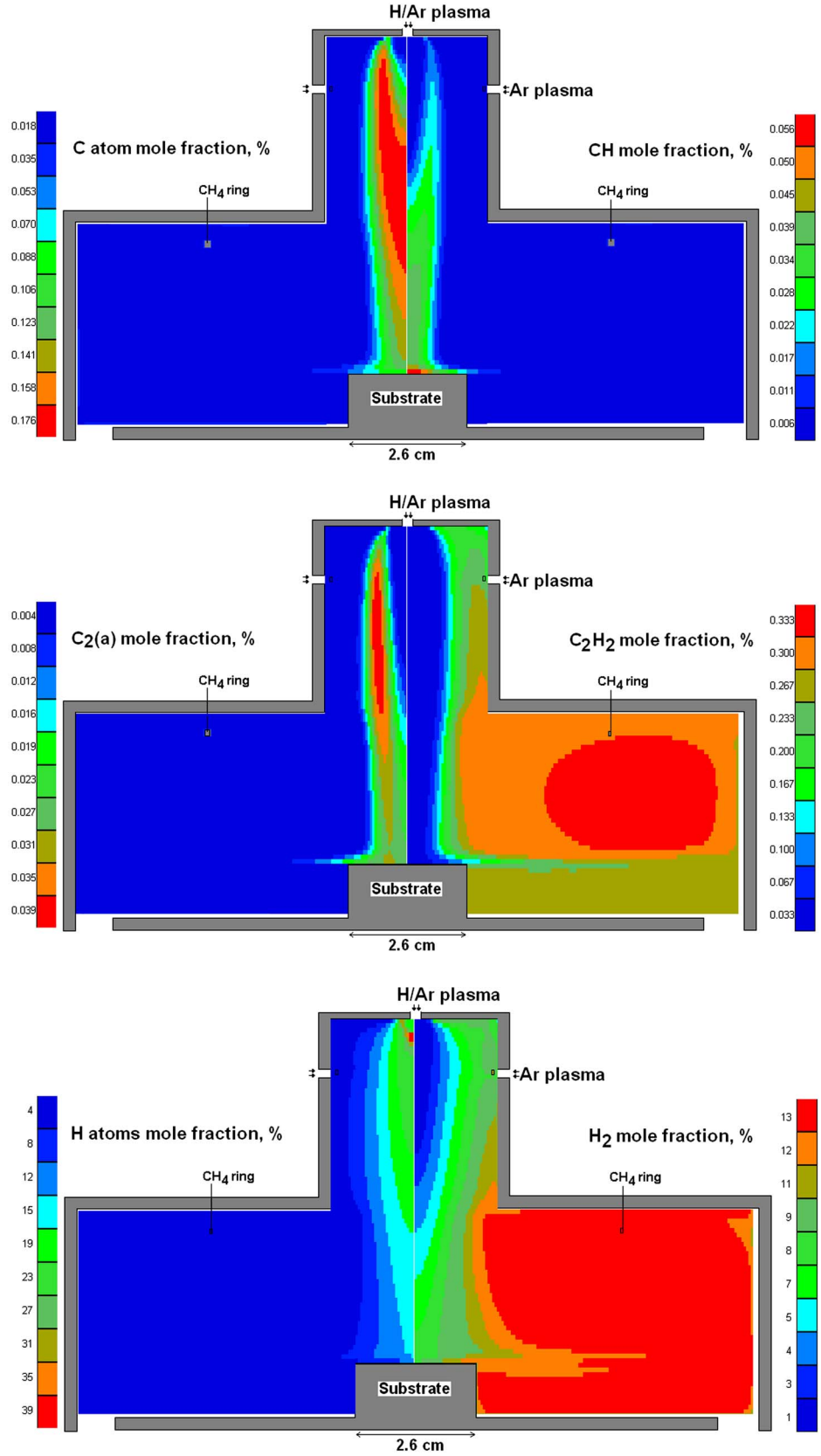

FIG. 2. Calculated two-dimensional percentage mole fraction profiles of selected important species C, CH, $C_2(a)$, C_2H_2, H, and H_2 for the Bristol arc jet reactor operating under standard base conditions. The profiles are each plotted for half the reactor and are symmetric about the center line. The nozzle and substrate are located, respectively, at the top and bottom centers of each figure.

heavier species. As a result, quasiequilibrium distributions of various hydrocarbon species are established in the vortex region. For our base conditions of reactor operation, typical calculated concentrations (in cm^{-3}) of the more abundant species in the central part of the vortex are as follows: $C_2H_2 \sim 1.2\times10^{15}$, $CH_4 \sim 4.5\times10^{13}$, $CH_3 \sim 1.3\times10^{13}$, $C_2H_4 \sim 5.7\times10^{12}$, $C_3 \sim 1.2\times10^{13}$, $C_3H_2 \sim 4.7\times10^{13}$, $C_4H_2 \sim 1.2\times10^{13}$, $H \sim 8.3\times10^{14}$, $H_2 \sim 4.5\times10^{16}$, and $Ar \sim 3\times10^{17}$. Upwind flow near the wall of the narrower bore section and species diffusional flows deliver H_2 molecules and various C_xH_y species back to the plume, where they are incorporated into the main stream and decompose into atoms (C and H) and simple molecules, e.g., CH and C_2, in regions of higher temperature ($T > 5000$ K) towards the center of the plume. An important reactive and highly nonequilibrated transition zone is observed at the boundary of the hot plume in computed two-dimensional distributions of C_2 (see Fig. 2) and other species such as C_2H and C_3. The fastest reactions with C_xH_y species in the plume and transition zone are the H-shifting reactions, such as

$$CH_y + H \leftrightarrow CH_{y-1} + H_2, \quad y = 1,2, \tag{13}$$

$$C_2H_y + H \leftrightarrow C_2H_{y-1} + H_2, \quad y = 1,2. \tag{14}$$

The acetylene diffuses radially towards the hotter plume core and is chemically processed first to C_2H and then C_2. Wills *et al.*[4] made cw diode laser carity ring down spectroscopy (CRDS) measurements of the acetylene content of the reactor, and demonstrated clearly that it is principally located in the cooler parts away from the plume and at number densities consistent with the model calculations. Various reactions involving the interconversion between CH_y, C_2H_y, C_3H_y, C_4H_y, and higher hydrocarbon species and thermal decompositions of C_xH_y species are slower (by one to several orders of magnitude in different regions of the reactor) than the H-shifting reactions. A consequence of the variety of local conditions (gas temperature, H, H_2, and C_xH_y concentrations) is that the chemical mechanism cannot be reduced to a limited number of prevailing exchange reactions; instead, we identify several important reactions of this type, including

$$C + C_2H \leftrightarrow C_3 + H, \tag{15}$$

$$C + C_2H_2 \leftrightarrow C_3H + H, \tag{16}$$

$$C + C_2H_2 \leftrightarrow C_3 + H_2, \tag{17}$$

$$C + C_3 \leftrightarrow C_2 + C_2, \tag{18}$$

$$C + CH \leftrightarrow C_2 + H, \tag{19}$$

$$C_2 + C_2H_2 \leftrightarrow C_4H + H, \tag{20}$$

$$C_2H + C_2H_2 \leftrightarrow C_4H_2 + H. \tag{21}$$

Thus, we observe a very complicated picture of C_xH_y transformation in the Bristol reaction chamber, which can be summarized as follows: in the vortex region, $CH_4 \rightarrow CH_3 \leftrightarrow C_2H_2 \leftrightarrow$ heavier hydrocarbons; in the plume and transition zone, $C_2H_x \leftrightarrow (CH_y \text{ and } CH_z)$, $C_3H_x \leftrightarrow (CH_y \text{ and } C_2H_z)$, $(C_2H_y \text{ and } C_2H_z) \leftrightarrow C_4H_x \leftrightarrow (CH_y \text{ and } C_3H_z)$. Depending on the local gas temperature T_g and the H/H_2 ratio, the H-shifting equilibria favor C, CH, and C_2 species (in the hot, H-rich axial region of the plume, with C dominant in the core of the plume, as would be expected at the high temperatures of this region) or CH_2, C_2H, and C_2H_2 species (at the outer boundary of the transition zone). As mentioned above, this pattern is violated in the plume regions where the concentrations $[H_2] \ll [Ar^+]$ or $[H_2] \ll [H^+]$ and ions affect the neutral C_xH_y transformations. These effects are discussed further in the accompanying paper,[1] where a detailed comparison of experimental data and the outputs of the full two-dimensional model is presented. The comparison includes much recent experimental data on spatial variations of the column densities of C_2 and CH radicals, as a function of process conditions, which provide more rigorous tests of the model than our prior measurements.

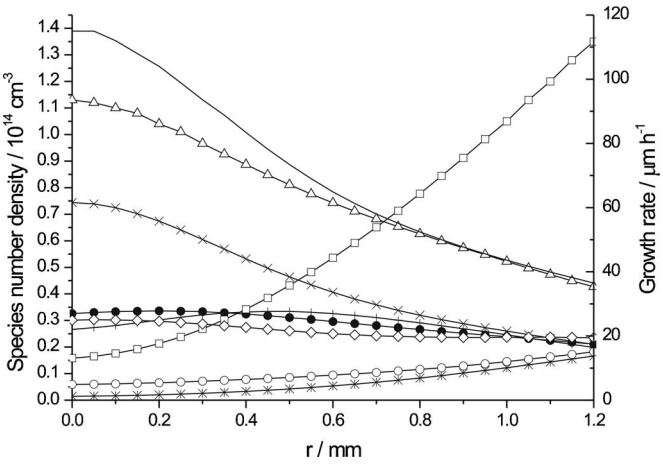

FIG. 3. Calculated radial distributions of the diamond film growth rate and CH_x species distributions just above the substrate. (△) C atoms, (×) CH, (●) $C_2(a)$, (+) C_2H, (□) C_2H_2, (∗) C_3, (○) CH_3, (◇) CH_2, and (−) Growth rate (right-hand axis).

The highly excited and reactive H/C/Ar plume mixture impinges on the substrate and induces very high, but radially nonuniform, film-deposition rates. Calculated species concentrations just above the substrate can be used to estimate the absolute values and radial variation of the diamond growth rates G [issue (iii) in the earlier list]. The model and derived formulae for G are described in detail in Ref. 19. The calculated radial profiles of the growth rate due to CH_y species, and the number densities of the most abundant C_xH_y species just above the substrate are shown in Fig. 3 for base reactor conditions ($F_{CH_4}{}^0 = 80$ SCCM, $F_{H_2}{}^0 = 1.8$ SLM) and a substrate temperature of 1200 K. The calculations assume that the chemical composition of the plume is not altered by the presence of a thin boundary layer, as discussed previously. C and CH are the most abundant C_xH_y species, and several others have significant abundances, most notably $C_2(a)$, C_2H, and CH_2, and must be considered as possible further contributors to the film growth. C_2H_2 dominates the gas-phase C_xH_y composition towards the periphery of the plume. The experimentally observed high growth rates, G

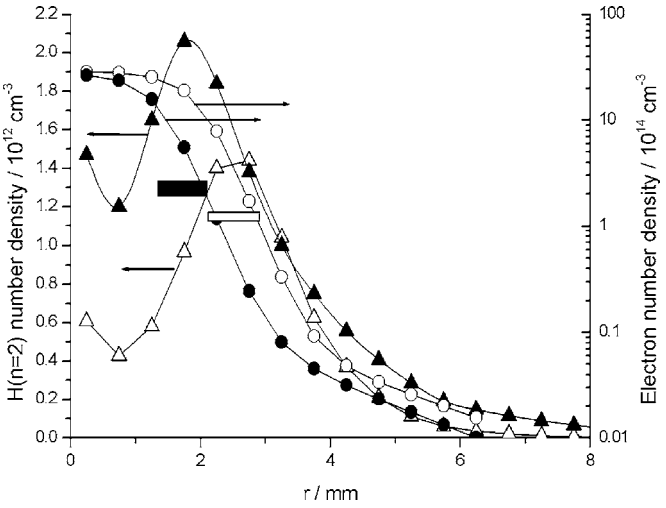

FIG. 4. Calculated radial profiles of H(n=2) (triangles) and electron (circles) number densities for the arc jet reactor operating with flows of methane of 0 SCCM (white symbols) or 80 SCCM (black symbols) and otherwise standard conditions. The arrows indicate the axes against which the data are plotted. The black and white boxes (with color coding as above) indicate approximate electron number densities that would be derived from Stark broadening measurements of the H atom Balmer-α or -β lines, which are sensitive to the electron densities in the regions of the plume where the H(n=2) number densities are greatest. In this example, the higher CH_4 flow rate gives rise to a higher apparent electron density (see text for further discussion).

$\sim$100 μm/h, could be accounted for, within the model of Ref. 19, simply in terms of the contributions of C_1H_x species. Calculations for other H_2 flow rates (500, 1000, and 1500 SCCM) show that the concentrations of CH and C atoms increase and decrease, respectively, with greater H_2 flow rate, but the total contribution of C_1H_x species and, thus, the modeled growth rate remain in the same general range (with $G \sim 40-150$ μm/h).

Figure 4 provides an explanation of an apparent paradox detected experimentally, denoted as (iv) in the earlier list: the deduced electron number density N_e increases with addition of hydrocarbon ions, which undergo fast recombination reactions. The measured N_e which is derived from Stark broadening of H Balmer-α or -β absorption lines, characterizes the off-axis region where the number density of H(n=2) maximizes. In this region, the electron number density is much lower than its maximum, on-axis value, and the measured value will be very sensitive to small ($\sim$1 mm) radial shifts of the position of the H(n=2) concentration maximum because of the very sharp radial gradients of N_e. Thus, as the calculations show, an apparent increase in N_e with CH_4 flow could be detected under conditions of an overall drop of N_e, if the addition of methane compresses the H(n=2) radial distributions to increase the overlap of the radial profiles of electron and H(n=2) number densities.

Figure 5 shows the calculated axial profiles of several neutral and charged species number densities at the plume centerline (r=0 mm) and at the plume boundary (r=6 mm). As is evident from the plots, many of the species number densities change by several orders of magnitude over the axial and radial extent of the plume, emphasising the above-mentioned complexity of plasma-chemical transformations within the plasma jet.

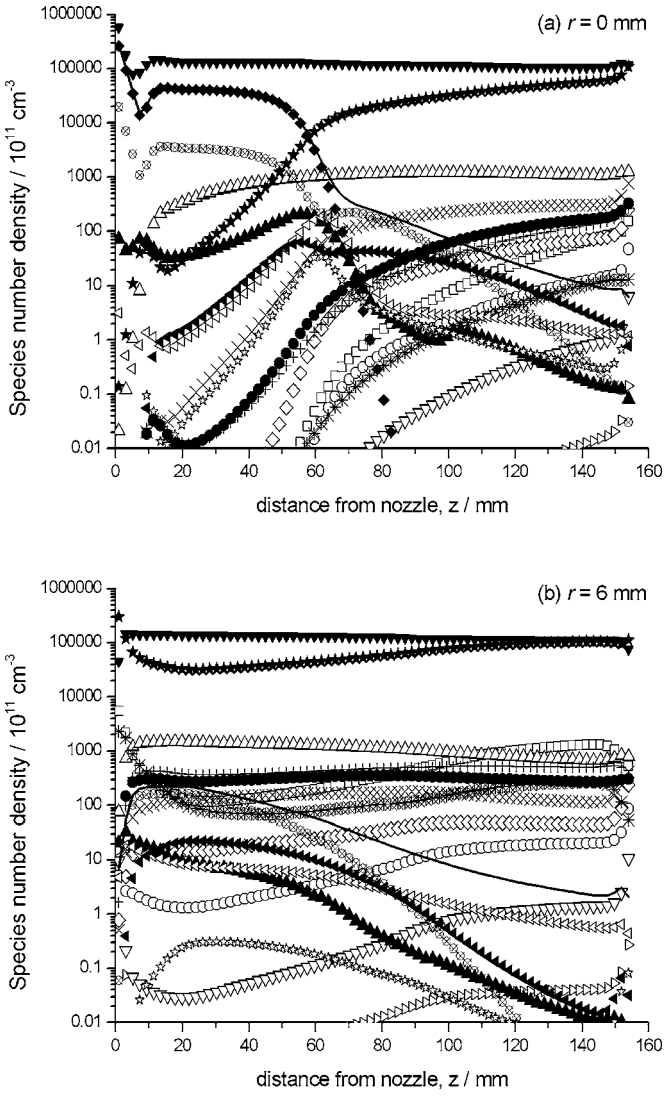

FIG. 5. Calculated z-dependent number density profiles at (a) r=0 and (b) r=6 mm for the Bristol dc arc jet reactor. Key: (△) C atoms, (×) CH, (●) $C_2(a)$, (+) C_2H, (□) C_2H_2, (∗) C_3, (○) CH_3, (◇) CH_2, (▼) H(n=1), (▲) H(n=2), (★) H_2, (▷) C_2H_4, (▽) CH_4, (−) e^-, (♦) Ar^+, (⊗) H^+, (◁) ArH^+, (◀) C^+, and (☆) H^-.

III. CALCULATIONS FOR THE SRI REACTOR

The modeling approach developed for the Bristol arc jet reactor was also used for simulation of the SRI International dc arc jet CVD reactor.[11–16] The SRI arc jet reactor has been intensively studied, with an abundance of experimental data collected on various aspects of characterization of the expanded plasma, including (r,z) distributions of gas temperatures and flow velocities;[13] CH, C_2, C_3, and H species number densities [determined by laser induced fluorescence (LIF)];[11] the degree of hydrogen dissociation (determined by a calorimetry method);[11] and excited state density distributions of H, C, CH, and C_2 (by optical emission spectroscopy).[15] In this lower power ($\sim$1600 W, $\sim$2 eV/molecule) arc jet, the dc discharge was struck through a mixture of Ar and H_2 (rather than in a pure Ar flow as in the Bristol arc jet reactor), and methane was added to the activated gas mixture through orifices in the diverging part of the nozzle. The boundary conditions and geometry of

the model reactor were thus specially adapted to reflect the different nozzle geometry in the SRI reactor (a nozzle throat diameter of 0.635 mm, with exit diameter of 9.53 mm, and a length of the diverging nozzle section of ~13 mm). A schematic diagram of the nozzle is available in Fig. 1 of Ref. 13.

Two-dimensional model calculations have been carried out for the following basic operational parameters of the SRI reactor: an H_2 flow rate of 3.27 SLM, an Ar flow rate of 3.63 SLM, a CH_4 flow rate of ~0.016 SLM, a dc arc discharge input power of 1.6 kW, a gas pressure of ~5300 Torr for the initial flow (upstream of the discharge), a gas pressure in the reaction chamber of 25 Torr, and a substrate temperature T_s=870 K. We first determined analytically the plasma parameters for the nozzle throat cross section using experimental measurements of power loss of 475±55 W into cooling water,[14] and assuming that additional (e.g., radiative[14]) power losses do not exceed 50 W. Contrary to the analysis in Ref. 14, we do not include the kinetic energy of the plasma stream (~410 W) in the energy balance considerations for the calorimetry method. The high, near speed-of-sound, flow velocities are a result of the pressure difference of the initial flow (pressure=5300 Torr) and the gas that has expanded in the reaction chamber (25 Torr), and would be observed without any discharge input power. According to Eqs. (1) and (8)–(12), the remaining 1075 W of input power into the flowing plasma results in the following plasma parameters at the nozzle throat: gas temperature T_{gas}~6000 K; gas pressure P~3700 Torr and flow velocity v_z=1600 m/s; and mole fractions X_H~0.34, X_{H2}~0.22, X_{Ar}~0.44. The low ionization degree (X_e<0.01% in the plume[14]) does not affect the gas flow parameters. The degree of hydrogen dissociation, $[H]/([H]+2[H_2])$~0.436 returned by the analytical approach of Eqs. (1) and (8)–(12) and calorimetry data, is much lower than the equilibrium degree of dissociation at 6000 K (~0.977). This deviation is probably due to the short residence time of the mixture in the hot dc discharge region and/or hydrogen atom recombination processes at the metal surfaces of the arc jet apparatus. It is difficult to make a more accurate assessment of the inlet plasma parameters, so we have instead varied these parameters and further unknown conditions for the diverging nozzle surface within limits of ±20% from the stated values, and showed that the calculated results remain stable and are not seriously affected by such uncertainties. For the present calculations, we took 2000 K as a basic value of the surface temperature of the diverging tungsten nozzle and γ=0.15 for the atomic hydrogen recombination probability on the nozzle surface and reaction chamber walls.

The calculated results are in qualitative and satisfactory quantitative agreement with experimental measurements of gas flow parameters and species concentrations profiles. For example, the calculated flow velocity v_z~2400 m/s at the plume center (r=0, z=20 mm) compares favorably with a measured value v_z~2600 m/s, and the calculated gas temperature T~2200 K is only slightly lower than that measured experimentally (T~2200–2400 K).[13] The calculated CH, C_2, and C_3 concentration profiles are compared with the LIF measurements of CH, C_2, and C_3 number densities distributions in Figs. 6 and 7. Figure 6 shows the species radial

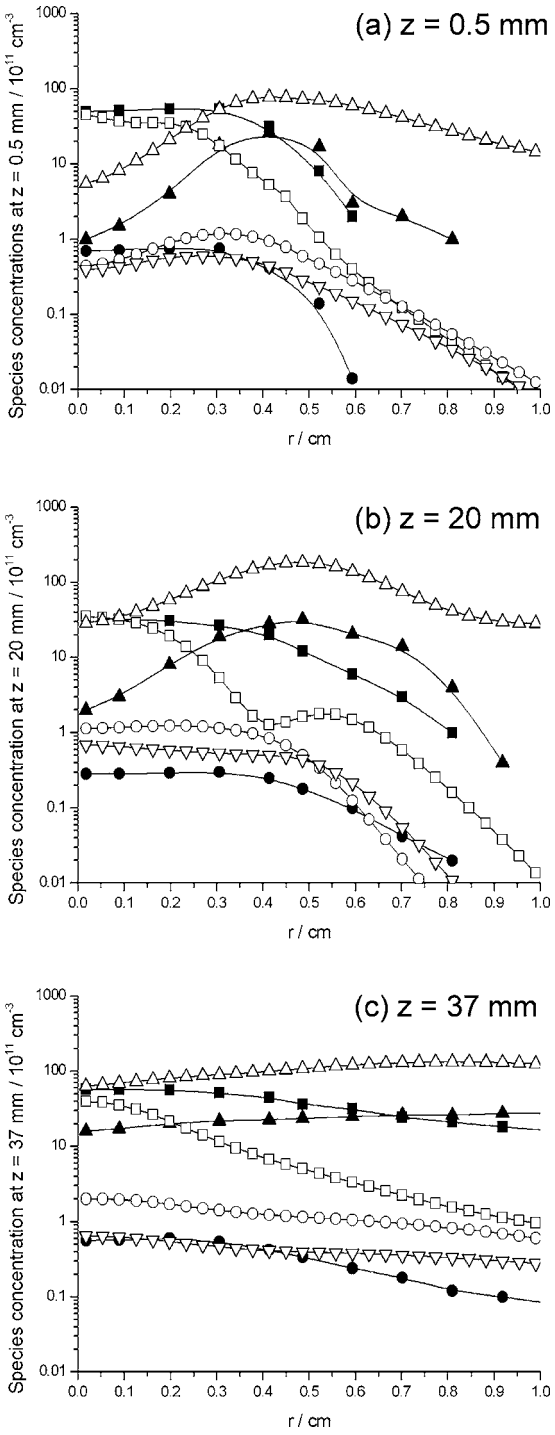

FIG. 6. Calculated and measured radial number density profiles of CH, C_2, and C_3 for the SRI dc arc jet reactor: (a) z=0.5 mm, near the nozzle exit; (b) z=20 mm, at the middle of the plume; and (c) z=37 mm, in the boundary layer above the substrate. Key: experimental, LIF measurements of CH (■), $C_2(a)$ (●), and C_3 (▲); model calculations of CH (□), $C_2(a)$ (○), C_3 (△), and $C_2(X)$ (▽).

profiles at three plume cross sections: near the nozzle exit (at an axial coordinate z=0), near the plume center (z=20 mm), and at 1.2 mm from the substrate (z=37 mm). In this coordinate system for the model reactor, the nozzle throat cross section and CH_4 injection ring nozzle were located at z=−13 mm and z=−10 mm, respectively. Reasons for the discrepancies in the measured and calculated profiles for CH at z=20 mm and around r=0.4 cm are not clear.

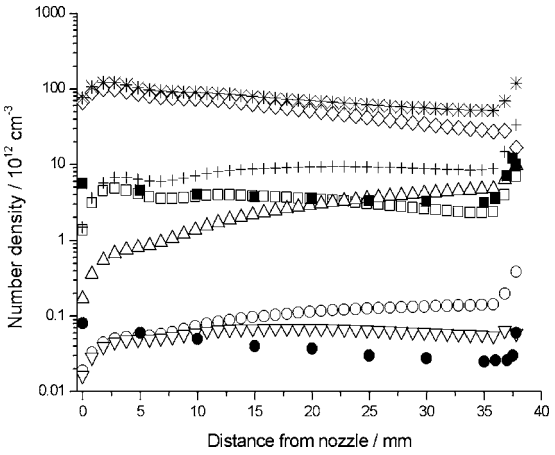

FIG. 7. Calculated and measured C_xH_y number densities on the centerline $(z,r=0)$ of the plasma plume in the SRI reactor. Key: experimental, LIF measurements of CH (■) and $C_2(a)$ (●); model calculations of C (◇), CH (□), $C_2(a)$ (○), C_3 (△), $C_2(X)$ (▽), CH_3 (∗), and CH_2 (+).

Calculated hydrogen concentrations were as follows: $[H] \sim 1.6\times10^{16}$ cm^{-3} and $[H_2]\sim 6.3\times10^{16}$ cm^{-3} at $z=0$ mm, and $[H]\sim 5.4\times10^{15}$ cm^{-3} and $[H_2]\sim 5.5\times10^{16}$ cm^{-3} at $z=20$ mm. The calculated atomic hydrogen concentrations are lower than the results of LIF measurements, which gave $[H]\sim 4\times10^{16}$ cm^{-3} at $z=0$ and $[H]\sim 2.5\times10^{16}$ cm^{-3} at $z=20$ mm. Figure 7 shows the axial variation of CH_y, $y=0-3$, C_2, and C_3 on the centerline of the plume. As is seen from species concentrations just above the substrate surface, $CH_{y=0-3}$ species are dominant, and the main diamond growth precursors in the SRI reactor are, thus, likely to be C, CH_2, and CH_3, with CH and C_3 also showing sharp rises in number density in proximity to the surface. For the SRI reactor, the gas flow conditions above the boundary layer (flow velocity $v_r\sim 10^5$ cm/s, gas density $\sim 10^{-5}$ g/cm^3, and gas temperature $\sim$2500–3000 K) ensure that the thermal boundary layer thickness is sufficiently thin $[\delta\,(\mathrm{cm}) \leqslant 0.08R_s^{1/2}$, with $R_s=0.65$ cm being the radius of the substrate holder] to use the calculated species concentrations above the boundary layer for analysis of growth mechanisms.

The growth rate G from CH_x $(x<4)$ radicals can be estimated[19] to be $G(r=0)\sim 9$ μm/h at a substrate temperature of $T_S=870$ K (as reported in ref. 24). This estimation uses calculated number densities of H atoms, $[H]\sim 6.2\times10^{15}$ cm^{-3} above the substrate center, $r=0$, and $[H]\sim 3\times10^{15}$ cm^{-3} above the substrate edge, $r=6$ mm, giving a ratio of $G(r=6)/G(r=0)$ of $\sim$0.25. The experimental growth rate in the SRI reactor was reported to be $G\sim 50$ μm/h under standard operating conditions,[14] but at an unspecified T_S. The difference in model and measured growth rates might, thus, in part be a consequence of different substrate temperatures: for $T_s=1200$ K, the estimated growth rate is instead $G=27$ μm/h, based on the current model outcomes for radical and atomic number densities above the substrate.

The refined plasma-chemical mechanism also offers an explanation of the results of optical emission spectroscopy (OES) measurements of the excited states of selected species.[15] Our calculations suggest that the main mechanism of electronic excitations in the SRI reactor is electron-ion recombination. For example, the rate of dissociative recombination of ArH^+ with an electron,

$$ArH^+ + e \leftrightarrow Ar + H(n>1), \tag{22}$$

is much higher (by many orders of magnitude) than the direct electronic excitation proposed in Ref. 15 as the predominant mechanism of formation of excited states of the H atoms.

IV. CONCLUSIONS

The approach developed for arc-jet CVD reactor simulations, described in detail in this paper, building on the content of Ref. 7, allows us to reproduce self-consistently many aspects of complex plasma-chemical and transport processes, not only in the Bristol dc arc jet reactor, but also in a similar, but lower power reactor operated and studied by Jeffries and co-workers at SRI, and for which extensive experimental measurements are available. Phase I of the model approach serves to determine accurately the plasma parameters (temperature, pressure, flow velocity, and degree of ionization and dissociation of an activated feedstock gas mixture) of the inlet high pressure gas flow. In the second and third phases, a two-dimensional model of the H/C/Ar plasma expanded into a low pressure chamber provides full characterization of all aspects of the gas-phase CVD processes: plasma-chemical kinetics, plume expansion and gas recirculation, radiation, heat and mass transfer, carbon feed gas decomposition, C_xH_y species transformation and diffusion, and potential diamond precursors capable of providing the extremely high growth rates ($\sim$100 μm h^{-1}). As a result, the model calculations allow us to explore and understand key features of the deposition process and to explain numerous experimental observations and results, including spatial distributions of C_xH_y number densities, gas temperatures, and flow velocities; excited $H(n>1)$ atom spatial profiles, the mechanisms of formation of species in excited electronic states, and associated OES measurement results; and to comment on diamond growth rates. The model calculations indicate that the experimentally observed high and nonuniform diamond growth rates are determined mainly by the contributions from C atoms and CH radicals in the high-power Bristol reactor, and CH_y (y=0–3) radical contributions in the lower power SRI reactor.

ACKNOWLEDGMENTS

We thank the EPSRC for the financial support for the Bristol group, the Royal Society for a Joint Project Grant, the ISTC for the award of Grant No. 2968/2005 (Yu.A.M.), and the RFBR for Key Science Schools Grant No. 7101.2006.2 (Yu.A.M.). We thank Dr. C.J. Rennick, J. Ma, J.J. Henney, and Dr. J.B. Wills for many valuable discussions, and Element Six, Ltd. for long-term support of the Bristol programme.

[1] C. J. Rennick, J. Ma, J. J. Henney, J. B. Wills, M. N. R. Ashfold, A. J. Orr-Ewing, and Yu. A. Mankelevich, J. Appl. Phys. **102**, 063309 (2007).
[2] J. B. Wills, J. A. Smith, W. E. Boxford, J. M. F. Elks, M. N. R. Ashfold, and A. J. Orr-Ewing, J. Appl. Phys. **92**, 4213 (2002).

[3]Y. A. Mankelevich, N. V. Suetin, M. N. R. Ashfold, W. E. Boxford, A. J. Orr-Ewing, J. A. Smith, and J. B. Wills, Diamond Relat. Mater. **12**, 383 (2003).
[4]J. B. Wills, M. N. R. Ashfold, A. J. Orr-Ewing, Y. A. Mankelevich, and N. V. Suetin, Diamond Relat. Mater. **12**, 1346 (2003).
[5]C. J. Rennick, J. A. Smith, M. N. R. Ashfold, and A. J. Orr-Ewing, Chem. Phys. Lett. **383**, 518 (2004).
[6]C. J. Rennick, A. G. Smith, J. A. Smith, J. B. Wills, A. J. Orr-Ewing, M. N. R. Ashfold, Yu. A. Mankelevich, and N. V. Suetin, Diamond Relat. Mater. **13**, 561 (2004).
[7]C. J. Rennick, R. A. H. Engeln, J. A. Smith, A. J. Orr-Ewing, M. N. R. Ashfold, and Yu. A. Mankelevich, J. Appl. Phys. **97**, 113306 (2005).
[8]C. J. Rennick, J. Ma, M. N. R. Ashfold, A. J. Orr-Ewing, and Yu. A. Mankelevich, Plasma Sources Sci. Technol. **15**, 432 (2006).
[9]M. E. Coltrin and D. S. Dandy, J. Appl. Phys. **74**, 5803 (1993).
[10]B. W. Yu and S. L. Girshick, J. Appl. Phys. **75**, 3914 (1994).
[11]J. Luque, W. Juchmann, and J. B. Jeffries, J. Appl. Phys. **82**, 2072 (1997).
[12]W. Juchmann, J. Luque, J. Wolfrum, and J. B. Jeffries, Diamond Relat. Mater. **7**, 165 (1998).
[13]W. Juchmann, J. Luque, and J. B. Jeffries, Appl. Opt. **39**, 3704 (2000).
[14]W. Juchmann, J. Luque, and J. B. Jeffries, J. Appl. Phys. **81**, 8052 (1997).
[15]J. Luque, W. Juchmann, and J. B. Jeffries, J. Vac. Sci. Technol. A **16**, 397 (1998).
[16]W. Juchmann, J. Luque, and J. B. Jeffries, Appl. Opt. **44**, 6644 (2005).
[17]Gri-Mech mechanism, http://www.me.berkeley.edu/gri_mech
[18]B. J. Wood and H. Wise, J. Phys. Chem. **65**, 1976 (1961).
[19]P. W. May, M. N. R. Ashfold, and Yu. A. Mankelevich, J. Appl. Phys. **101**, 053115 (2007).
[20]B. V. Alekseev and A. M. Grishin, *Physical Gas Dynamics of Reactive Flows*, High School ed. (High School, Moscow, 1985).
[21]D. S. Dandy and M. E. Coltrin, J. Mater. Res. **10**, 1993 (1995).
[22]Yu. P. Raizer, *Gas Discharge Physics* (Nauka, Moscow, 1987).
[23]S. Mazouffre, M. G. H. Boogaarts, I. S. J. Bakker, P. Vankan, R. Engeln, and D. C. Schram, Phys. Rev. E **64**, 016411 (2001).
[24]J. Luque, W. Juchmann, and J. B. Jeffries, Appl. Opt. **36**, 3261 (1997).
[25]See EPAPS Document No. E-JAPIAU-102-096718 for details of the chemical mechanism used in the computer model. This document can be reached via a direct link in the online article's HTML reference section or via the EPAPS homepage (http://www.aip.org/pubservs/epaps.html).